ARTICLE

Experimental and Theoretical Study on *p*-Chlorofluorobenzene in the S_0, S_1 and D_0 States

Jia-nan Fan, Ting-ting Cui, Zheng-bo Qin*, Xian-feng Zheng*, Zhi-feng Cui

Anhui Province Key Laboratory of Optoelectric Materials Science and Technology, Department of Physics, Anhui Normal University, Wuhu 241000, China

(Dated: Received on January 8, 2020; Accepted on February 19, 2020)

The geometric structures and vibration frequencies of *para*-chlorofluorobenzene (*p*-ClFPh) in the first excited state of neutral and ground state of cation were investigated by resonance-enhanced multiphoton ionization and slow electron velocity-map imaging. The infrared spectrum of S_0 state and absorption spectrum for $S_1 \leftarrow S_0$ transition in *p*-ClFPh were also recorded. Based on the one-color resonant two-photon ionization spectrum and two-color resonant two-photon ionization spectrum, we obtained the adiabatic excited-state energy of *p*-ClFPh as 36302±4 cm^{-1}. In the two-color resonant two-photon ionization slow electron velocity-map imagin spectra, the accurate adiabatic ionization potential of *p*-ClFPh was extrapolated as 72937±8 cm^{-1} via threshold ionization measurement. In addition, Franck-Condon simulation was performed to help us confidently ascertain the main vibrational modes in the S_1 and D_0 states. Furthermore, the mixing of vibrational modes between $S_0 \rightarrow S_1$ and $S_1 \rightarrow D_0$ has been analyzed.

Key words: Resonance-enhanced multiphoton ionization, Slow electron velocity-map imaging, Duschinsky mixing, *para*-Chlorofluorobenzene

I. INTRODUCTION

Halogenated hydrocarbons, which play a vital role in the human life, are the important raw materials of pesticides, refrigerants, fire extinguishers, chemical dyes and so on. However, the derivatives of halogenated hydrocarbons are highly toxic, quite stable and hard degradation [1]. They can be enriched in animals through the food chain, which will cause the accumulation of residues and endanger human health and ecological environment, such as carcinogenesis [2], destruction of the ozone layer [3], and so on. Chlorinated hydrocarbons are ubiquitous pollutants that exist in the environment as herbicide, preservative, and disinfectant [4]. Some chlorinated aromatic hydrocarbons are widely used in medicine, industry, and agriculture [5]. They also commonly exist in potable water as disinfection because of chlorination [6]. In addition, many chlorinated hydrocarbons are extremely stable and easy to accumulate [7]. The photodissociation dynamics of halogenated aromatic hydrocarbons is closely related to atmospheric chemistry and has practical significance for environmental protection, especially in the protection of ozone layer [8].

In recent decades, many new techniques have been used in the experimental and theoretical studies on halogenated hydrocarbons. Murakami *et al.* [9] studied the fluorobenzene and chlorobenzene by means of multi-photoionization technology to obtain the two-photon absorption spectra. Gaber *et al.* [10] drew conclusion that the argon atom shifted towards the chlorine atoms during excitation for the *ortho*- and the *meta*-isomer while it stayed in the middle of the ring for the *para*- isomer from the REMPI spectra, and obtained the binding energy in the ground state of ion from the MATI spectra. Borg *et al.* [11] used femtosecond laser spectroscopy and high order *ab initio* CASCF/CASPT2 quantum chemical calculation to study the photochemistry of six different fluorobromobenzene compounds with low excited states, and discussed the influence of the position and number of substituents on the dissociation mechanism and degree of bromobenzene. In addition, the quantum chemical calculations of the potential energy surfaces of monohalogenated benzene [12], dibromobenzene [13], bromofluorobenzene [14] and 1,3,5-tribromobenzene [15] showed that the main dissociation channels involved excitation from the lowest excited singlet (non-localized ($\pi\pi^*$) state to the triple antibond ($\pi\sigma^*$ or $n\sigma^*$)) state on the C−X bond. Liu *et al.* combined the femtosecond pump-probe method with time-of-flight mass spectroscopy and photoelectron velocity mapping technique to study the photodissociation dynamics of o-dichlorobenzene in its lowest excited singlet state [16].

Recently, resonance-enhanced multiphoton ionization

*Authors to whom correspondence should be addressed. E-mail: wave0403@163.com, xfzheng@mail.ahnu.edu.cn

(REMPI) and slow electron velocity-map imaging (SEVI) based on laser technology have become powerful tools to obtain the information of excited and cationic electronic states of molecules [17–19]. The advantages of this technique which is widely used in the study of vibrational energy levels of aryl molecules are high resolution and high efficiency. For example, Hammond *et al.* [17] applied SEVI to the experiment of molecular spectroscopy and dynamics of toluene. Its resolution can be comparable to ZEKE spectroscopy.

A number of halogenated hydrocarbons and their derivatives have been studied recently. Typically, it was reported that the dissociation of *ortho*-, *meta*-, and *para*-chlorofluorobenzene and their van der Waals clusters in supersonic jets were studied via the combination of REMPI and time of flight (TOF) mass spectrometry by Numata *et al.* [20]. Tuttle *et al.* investigated the $S_1 \leftarrow S_0$ electronic transition of *p*-ClFPh via REMPI spectroscopy [21]. The adiabatic ionization potential (AIP) of *p*-ClFPh was 9.011±0.008 eV, which was reported through the equilibrium measurement method in 1978 [22]. In addition, Kemp *et al.* reported AIP of *p*-ClFPh as 9.0408±0.0006 eV and analyzed the vibrational structures in ZEKE spectra [23]. In 2018, our group reported the vibrations of meta-bromofluorobenzene in the first excited state (S_1) and the cationic ground state (D_0), also gave the adiabatic excited-state energy and AIP [24]. Meanwhile, in view of a lack of unambiguously vibrational modes in S_0 state and UV absorption spectra nature of *p*-ClFPh, which could be useful for the environmental monitoring, we also have performed the infrared and UV absorption spectra studies on *p*-ClFPh.

II. EXPERIMENTS

The experimental apparatus consists of a self-made time-of-flight mass spectrometer and velocity map imaging spectrometry which has been reported previously [25]. *p*-ClFPh (99%) purchased from JK Scientific was used without further purification. A supersonic molecular beam was produced by expanding the sample seeded in argon (99.999%) with a backing pressure of 4 bar through the orifice (0.5 mm diameter) of a pulsed valve (Parker, General Valve series 9) running at 10 Hz. After collimation by the skimmer with a 0.5 mm diameter, the *p*-ClFPh supersonic molecular beam entered the interaction region between the repeller and extractor plates.

Two different dye lasers were used to excite and ionize the molecules. The excitation laser pulse (ω_1) was generated by frequency-doubled of the dye laser output (Sirah) pumped by the second harmonic output of Nd:YAG laser (Spectra-Physics). The ionization laser pulse (ω_2) was generated by frequency-double of the output of dye laser (ND6000, Continuum) pumped by Nd:YAG laser (Powerlite Precision II, Continuum). Coumarins 540A and 503 were used to ionize *p*-ClFPh. The laser bandwidth was approximate by 0.2 cm^{-1}, and the duration of the laser pulse was about 6−8 ns. Calibration of the fundamental wavelength was done with the wavemeter (SHR, Solarlaser, ∼0.1 cm^{-1}).

The one-color two-photon ($2\omega_1$) experiment was performed using a tunable frequency-doubling dye laser (Sirah). The two-color two-photon ($\omega_1+\omega_2$) experiment was performed near the $S_1 \leftarrow S_0$ transition of *p*-ClFPh using a tunable frequency-doubling dye laser (Sirah) and another dye laser (ND6000, Continuum). The produced ions were perpendicularly accelerated by time-of-flight mass spectrometry. Ion signals were accumulated and analyzed by a multichannel scaler (MCS, SRS, SR245). The time-gated mass spectra were averaged for 100 laser shots for each wavelength. In addition, wavelength was scanned at 0.3 cm^{-1} spacing. The region below 565 cm^{-1} was recorded as a two-color spectrum, with the ionizing photon being 37978 cm^{-1}, while the remainder of the spectrum was recorded as a one-color spectrum. This was necessary as it is impossible to ionize via the $S_1 \leftarrow S_0$ transition in a (1+1) REMPI scheme in the first region of ∼350 cm^{-1} [20].

In the two-color two-photon ($\omega_1+\omega_2$) ionization experiment, the pulse energy of the excitation laser (ω_1) was held below 10 μJ to prevent the one-color two-photon ionization process. The photoelectron signal was practically absent when only one of two laser pulses was applied to the system. Both laser pulses were linearly polarized with their **E** vectors perpendicular to the time-of-flight axis. The delay time between the excitation laser, the ionization laser and the pulse valve were controlled by two digital delay/pulse generators (DG535, SRS). Photoelectrons were accelerated along the time-of-flight axis in the velocity mapping condition and projected onto a home-made position-sensitive detector (50 mm diameter) coupled with a personal computer-interfaced CCD camera (Basler Scott, 782×582 pixels) system in conjunction with the photo-counting mode software interface embedded in LabVIEW code. The SEVI images were taken at low electric field condition (38 V/cm), and reconstructed through the BASEX program [26].

Infrared spectra of liquid phase were measured at room temperature. The infrared spectra of *p*-ClFPh were recorded using a FT-IR spectrometer (Vector 36, Brucker) at 0.4 cm^{-1} resolution and equipped with potassm bromide window. The UV absorption spectra were achieved from SHIMADZU UV-3600Plus. The resolution of UV-3600Plus is 0.1 nm. The *p*-ClFPh was dissolved in ethanol, and the concentration was 1.9×10^{-7} mol/L.

The infrared and absorption spectrum were simulated by the Gaussian 09 program package [27]. Geometry optimization and harmonic vibrational frequency calculations of *p*-ClFPh in the S_0, S_1, and D_0 states were also performed via the Gaussian 09 program package. The B3LYP method was adopted for the calculations of S_0 and D_0 states [28], while the method with con-

DOI:10.1063/1674-0068/cjcp2001005

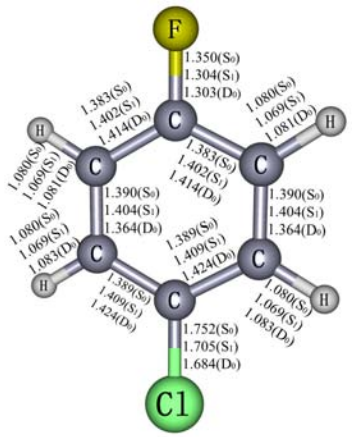

FIG. 1 Geometric configuration and labeling of the atoms for *p*-ClFPh in neutral ground state S_0 and ionic ground state D_0 using the optimized B3LYP/aug-cc-pVTZ structure, and first excited state S_1 at the level of RCIS-B3LYP/aug-cc-pVTZ.

figuration interaction singles (CIS) was applied to the S_1 state. The basis set aug-cc-pVTZ was utilized in all the optimized calculations. The stationary points were characterized as the energy minimum by verifying that all the corresponding frequencies were real. The calculated vibrational frequencies were scaled by a certain factor to approximately correct the combined errors stemming from the basis-set incompleteness and vibrational anharmonicity. Moreover, the FC-Lab II suite of programs has been utilized to predict the vibrational intensity distribution in the REMPI and SEVI spectra of *p*-ClFPh [29] in order to assign the vibrational modes [30]. The resulting REMPI and SEVI stick spectra have been convoluted by a lorentzian profile with a FWHM of 4 cm^{-1} in REMPI spectrum and 8 cm^{-1} in SEVI spectrum, respectively. The vibrational modes of S_1 and D_0 states in *p*-ClFPh were compared with the ones of S_0 state in *p*-ClFPh, respectively, via a generalized Duschinsky matrix approach using FC-Lab II.

III. RESULTS AND DISCUSSION

A. Geometry and molecular orbital

FIG. 1 shows the optimized structures of *p*-ClFPh in S_0, S_1 and D_0 states. The *p*-ClFPh with thirty normal modes belongs to the C_{2v} point group and the Cartesian coordinates are generalized in Table S1 (supplementary materials). The theoretical frequencies and experimental vibrations for S_0, S_1 and D_0 states are listed in Table S2 (supplementary materials) for comparison. A scaling factor of 0.97 is used. Numerous studies have shown that a great number of $S_1 \leftarrow S_0$ transitions mainly correspond to the electron-excited $\pi^* \leftarrow \pi$ transitions as shown in FIG. 2. Specifically, LUMO←HOMO transition of *p*-ClFPh mainly contributes to $S_1 \leftarrow S_0$ transition that corresponds to the excitation of $\pi^* \leftarrow \pi$. As a consequence, the weakening of the π bond leads to the expansion of the aromatic ring in S_1 state.

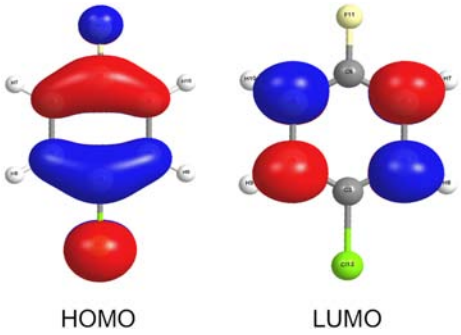

FIG. 2 The highest occupied molecular orbitals (HOMO) and lowest unoccupied molecular orbitals (LUMO) for *p*-ClFPh.

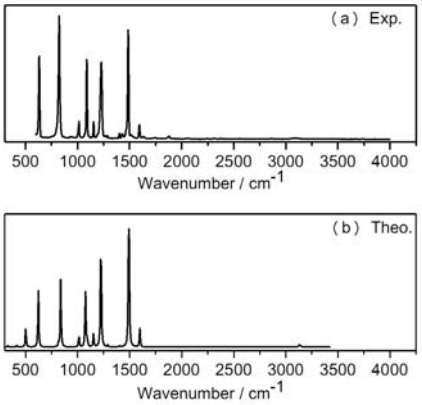

FIG. 3 Infrared spectrum of *p*-ClFPh: (a) experimental values, and (b) theoretical values with a scaling factor of 0.97.

B. Infrared spectrum of *p*-ClFPh

The infrared spectrum of *p*-ClFPh is obtained through the FT-IR spectrometer and compared with the simulated infrared spectrum at the level of B3LYP/aug-cc-pVTZ. The theoretical results are in excellent agreement with the experimental ones as shown in FIG. 3. The intense peaks appearing at 632, 823, 1088, 1229 and 1487 cm^{-1} well match theoretical values of 624, 829, 1082, 1212 and 1477 cm^{-1}. The weak peaks appear at 1012, 1152, 1267, 1286, 1402, 1593, 3076, and 3103 cm^{-1}, agreeing well with the calculated ones of 1002, 1141, 1274, 1278, 1389, 1583, 3099, and 3103 cm^{-1}. The peaks located at 632, 1012, 1088, and 1152 cm^{-1} are associated with the vibrations of the benzene ring, and the specific descriptions of the vibrations are summarized in Table S3 (supplementary materials).

C. Electronic absorption spectra of *p*-ClFPh

In order to determine the low-lying excited state of *p*-ClFPh, both TD-B3LYP and CIS with a basis set

DOI:10.1063/1674-0068/cjcp2001005

TABLE I Experimental and calculated absorption wavelength (λ), excited-state energies (E) and oscillator strengths (f) of *p*-ClFPh using TD and CIS methods and aug-cc-pVTZ basis set.

λ/nm			E/eV	f/a.u.	Major contributions[a]
Expt.		Calc.			
244	TD-B3LYP	246.98	5.02	0.0219	H→L(81)
		217.10	5.71	0.0938	H→L+2(79)
208		202.81	6.11	0.0050	H→L+3(63), H→L+2(32)
		191.43	6.48	0.0011	H→L+5(86)
		189.75	6.53	0.3927	H−1→L+1(74)
		181.25	6.84	0.0021	H−2→L(99)
		174.35	7.11	0.0003	H→L+7(94)
	CIS	209.86	5.91	0.0262	H→L+6(63)
		203.64	6.09	0.0038	H−1→L+6(39), H→L+5(23)
		183.56	6.75	0.0049	H→L(67)
		174.96	7.09	0.0012	H→L+4(23)
		170.23	7.28	1.0080	H−1→L+5(54), H→L+6(22)
		168.02	7.38	1.5023	H−1→L+6(46), H→L+5(21)
		166.75	7.44	0.0162	H→L+2(62)
		157.66	7.86	0.0448	H−1→L+1(71)
		156.97	7.90	0.0564	H→L+5(49), H→L+13(27)
		152.29	8.09	0.0019	H→L+7(34), H→L+8(21)

[a] H=HOMO, L=LUMO, H−1=HOMO−1, *etc.*

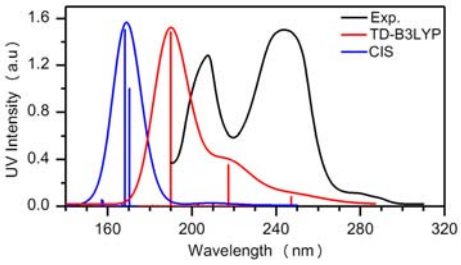

FIG. 4 Experimental and simulated UV absorption spectra of *p*-ClFPh in ethanol solution.

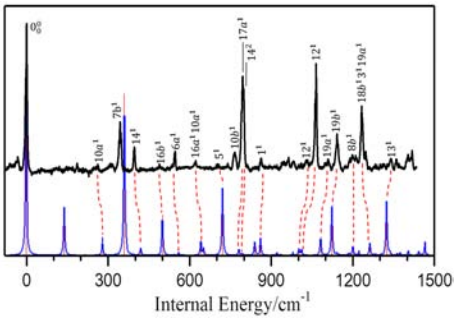

FIG. 5 The experimental spectrum and Franck-Condon simulated spectrum of *p*-ClFPh within ∼1500 cm^{-1} upon the S_1←S_0 electronic transition. The band origin of *p*-ClFPh is located at 36302 cm^{-1}.

of aug-cc-pVTZ calculations are performed to compare with the experimental results. FIG. 4 shows the experimental and theoretical UV absorption spectra in the range of 140−320 nm. In the experiment we observe the absorption peaks at 244 and 208 nm. The calculated vertical excited-state energies, oscillator strengths (f) and wavelengths are given in Table I. The TD-B3LYP calculation for *p*-ClFPh yields three electronic transitions (f>0.01) in this energy window: the first one is 189.75 nm (f=0.3927), the second one with moderate oscillator strength is located at 217.10 nm (f=0.0938) and the third one with lower oscillator strength is located at 246.98 nm (f=0.0219). The CIS computation predicts six electronic transitions (f>0.01): there are two strong ones distributed at 168.02 nm (f=1.5023) and 170.23 nm (f=1.0080), the other four absorptions (f>0.01) with lower oscillator strength are located at 156.97 nm (f=0.0564), 157.66 nm (f=0.0448), 209.86 nm (f=0.0262) and 166.75 nm (f=0.0162), respectively. The Multiwfn program is used to analyze the main contributions of the orbital transitions [31]. According to the absorption spectrum, the first absorption band is mainly assigned to the transition of LUMO←HOMO (near 81% using the TD-DFT method and 67% using CIS method).

D. Vibronic spectrum of *p*-ClFPh

FIG. 5 shows the spectrum of *p*-ClFPh ranging from 0 to 1400 cm^{-1} in S_1 state. The origin of the S_1←S_0 transition is established at 36302±4 cm^{-1}. The result

DOI:10.1063/1674-0068/cjcp2001005

TABLE II The comparison of experimental and calculated normal modes observed in the S_1 state of *p*-ClFPh.

Mode[a]	Major contributions from S_0[b]	Mixed Wilson (S_0)	Peak wavenumber/cm^{-1}	
			Expt.	Theo.[c]
Q'_1	$0.97\times Q_6$	16a		71
Q'_2	$0.99\times Q_1$	11^1		110
Q'_3	$0.99\times Q_3$	$10a^1$	261	275
Q'_4	$1.00\times Q_2$	$9a^1$		281
Q'_5	$0.99\times Q_4$	$7b^1$	344	365
Q'_6	$0.92\times Q_5$	14^1	396	428
Q'_7	$0.96\times Q_7$	$16b^1$	488	511
Q'_8	$0.91\times Q_9$	$6a^1$	546	585
Q'_9	$0.14\times Q_{10}$, $0.84\times Q_{11}$	$10a^1$ ($16a^1$)		599
Q'_{10}	$0.76\times Q_{10}$, $0.14\times Q_{11}$	$16a^1$ ($10a^1$)	623	601
Q'_{11}	$0.99\times Q_8$	$6b^1$		660
Q'_{12}	$0.96\times Q_{15}$	5^1	703	676
Q'_{13}	$0.99\times Q_{13}$	$10b^1$	765	750
Q'_{14}	$0.96\times Q_{14}$	$17a^1$	795	813
Q'_{15}	$0.98\times Q_{12}$	1^1	863	850
Q'_{16}	$0.91\times Q_{16}$	12^1	1033	1036
Q'_{17}	$0.91\times Q_{18}$	$19a^1$	1109	1104
Q'_{18}	$0.92\times Q_{17}$	$19b^1$	1142	1136
Q'_{19}	$0.96\times Q_{19}$	$8b^1$	1197	1203
Q'_{20}	$0.08\times Q_{18}$, $0.36\times Q_{22}$, $0.52\times Q_{26}$	$18b^1$ (3^1, $19a^1$)	1232	1214
Q'_{21}	$0.93\times Q_{20}$	13^1	1340	1340
Q'_{22}	$0.44\times Q_{22}$, $0.21\times Q_{23}$, $0.26\times Q_{26}$	3^1 ($18b^1$, $18a^1$)		1416
Q'_{23}	$0.69\times Q_{23}$, $0.14\times Q_{26}$	$18a^1$ ($18b^1$)		1446
Q'_{24}	$0.99\times Q_{24}$	$18b^1$		1535
Q'_{25}	$0.98\times Q_{25}$	$9b^1$		1662
Q'_{26}	$0.81\times Q_{21}$, $0.15\times Q_{22}$	$18a^1$ (3^1)	1760	
Q'_{27}	$0.99\times Q_{28}$	$7a^1$		3273
Q'_{28}	$0.96\times Q_{27}$	$20b^1$		3280
Q'_{29}	$1.00\times Q_{29}$	$20a^1$		3291
Q'_{30}	$0.94\times Q_{30}$	2^1	3295	

[a] Normal modes of *p*-ClFPh in the S_1 state.
[b] Normal modes of *p*-ClFPh in the S_0 state.
[c] The scaling factor for the frequencies was 0.97.

agrees well with the result reported by Tuttle *et al.* (36275±2 cm^{-1}) [21]. Cvitaš *et al.* observed the value of band origin at 36275.10 cm^{-1} [32]. Numata *et al.* measured the band origin at 36272 cm^{-1} in the fluorescence excitation spectrum [20]. These reported values are close to our measured value. The S_1 band assignment based on RCIS with a basis set of aug-cc-pVTZ is quite appropriate in Table II, as the theoretical values well match with the experimental ones.

The intense peaks appearing at 344 and 795 cm^{-1} are in good agreement with the previously reported values of 344 and 795 cm^{-1} [33], which are allocated to modes $7b^1$ and $17a^1$ (see Table S4 in supplementary materials). To observe 795 cm^{-1} band, we see that there are two intense bands here. Tuttle *et al.* assigned the $9^1/29^2$ vibrational modes in *para*-fluorotoluene [33], which prompts us to consider the similar situation herein. In fact, we can identify the 14^1 transition at 396 cm^{-1}, and then the 14^2 transition is expected to be close to $17a^1$, so the peak at 795 and 799 cm^{-1} are possibly assigned to modes $17a^1$ and 14^2.

The weak bands appearing at 261, 396, 546, 765, 863, 1142 and 1340 cm^{-1} agree with previously reported values of 265, 397, 546, 762, 861, 1139 and 1342 cm^{-1} [33], which are assigned to the modes $10a^1$, 14^1, $6a^1$, $10b^1$, 1^1, $19b^1$ and 13^1 (see Table S4 in supplementary materials). Besides these peaks, some extremely weak bands are also identified through Franck-Condon simulation. The peaks located at 488, 703, 1109 and 1197 cm^{-1} are tentatively assigned to the modes $16b^1$, 5^1, $19a^1$ and

DOI:10.1063/1674-0068/cjcp2001005

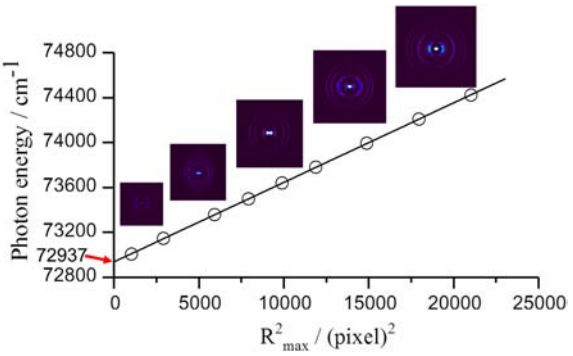

FIG. 6 The total photon energy was expressed as the squares of the radial positions of the corresponding 0^0 peak of the *p*-ClFPh cation. Data points were marked with empty circles. The linear regression can extrapolate this peak position to a zero radius, thereby the AIP is derived by the arrow.

$8b^1$. Additionally, we firstly mark the peak at 1033 cm^{-1} as mode 12^1. We also find that the combination vibrations of $16a^1(10a^1)$ and $18b^13^1(19a^1)$ occur at 623 and 1232 cm^{-1} through Franck-Condon simulation. The positions and relative intensities of these bands are well reproduced by Franck-Condon simulation to confirm the above assignment in FIG. 5.

E. Spectra of *p*-ClFPh cation

We determine AIP through extrapolation to the ionization threshold according to the formula:

$$kr_{\max}{}^2 = h\nu_{\text{pump}} + h\nu_{\text{probe}} - \text{AIP} \qquad (1)$$

where $r_{\max}$ is the radial distance corresponding to the maximum photoelectron kinetic energy (being associated with $D_0 \leftarrow S_1$ origin transition), $h\nu_{\text{pump}}$ is the energy of the pump photon, $h\nu_{\text{probe}}$ is the energy of the probe photon, and the AIP is the adiabatic ionization potential. As shown in FIG. 6, it can be inferred from the vertical intercept that the AIP is 72937±8 cm^{-1} ((9.0428±0.0010) eV). The measured value agrees fairly well with the previously reported one [23].

FIG. 7(a−g) show SEVI spectra of *p*-ClFPh recorded at seven different ionization wavelengths. The distribution of the vibrational level in the D_0 state is performed by comparing the experimental with calculated vibrational frequencies which are listed in Table III (all vibrational mode descriptions for S_0, S_1, and D_0 states of *p*-ClFPh are summarized in Table S2 in supplementary materials). In order to ascertain the experimentally observed frequencies, Franck-Condon simulation is predicted for comparison as shown in FIG. 8. Based on Franck-Condon analysis, the position and vibrational intensity of theoretical simulation are in general agreement with the experimental results, and the vibrational mode distributions of *p*-ClFPh cation in D_0 state are given. The intense peaks appearing at 382, 765, 832

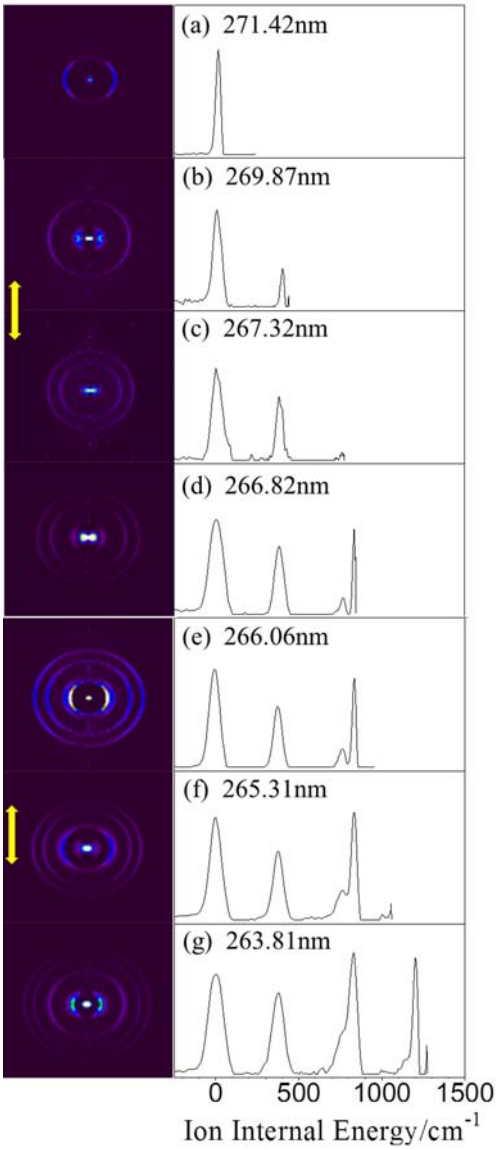

FIG. 7 2C-R2PI SEVI images (left column) and corresponding spectra (right column) of *p*-ClFPh. After the ionization of *p*-ClFPh in the 0_0^0 level in S_1, the recorded ionization wavelength is (a) 271.42 nm, (b) 269.87 nm, (c) 267.32 nm, (d) 266.82 nm, (e) 266.06 nm, (f) 265.31 nm, (g) 263.81 nm. The photoelectron images are reconstructed images by inverse Abel transformation. The double arrows indicate the directions of the laser polarization.

and 1200 cm^{-1} agree with previously reported values of 373, 782, 821 and 1176 cm^{-1}, which are allocated to modes $7b^1$, $10a^1$, $10b^1$ and $18a^1$. Besides, weak bands located at 645 and 1140 cm^{-1} agree with previously reported values of 658 and 1122 cm^{-1}, which are tentatively assigned to modes $6b^1$ and $8b^1$. The position and relative intensity of these bands are well reproduced by Franck-Condon simulation to confirm the above assignment (FIG. 8). These observed frequencies are also summarized in Table III. Besides these peaks,

DOI:10.1063/1674-0068/cjcp2001005

TABLE III The comparison of experimental and calculated normal modes observed in the D_0 state of *p*-ClFPh.

Mode[a]	Major contributions from S_1[b]	Mixed Wilson (S_1)	Peak wavenumber/cm^{-1}	
			Expt.	Theo.[c]
Q'_1	$0.99\times Q_2$	$9a^1$		268
Q'_2	$1.00\times Q_4$	$7b^1$	382	370
Q'_3	$1.00\times Q_3$	$10a^1$		270
Q'_4	$0.98\times Q_1$	11^1		100
Q'_5	$1.00\times Q_5$	14^1	419	412
Q'_6	$0.96\times Q_6$	$16a^1$		358
Q'_7	$0.98\times Q_7$	$16b^1$		497
Q'_8	$0.97\times Q_8$	$6b^1$	645	639
Q'_9	$1.00\times Q_{11}$	$10a^1$	765	774
Q'_{10}	$0.14\times Q_9$, $0.78\times Q_10$	$16a^1$ ($6a^1$)	702	
Q'_{11}	$0.79\times Q_9$, $0.13\times Q_10$	$6a^1$ ($16a^1$)	591	573
Q'_{12}	$1.00\times Q_{15}$	5^1		977
Q'_{13}	$0.98\times Q_{13}$	$10b^1$	832	855
Q'_{14}	$0.99\times Q_{16}$	12^1		965
Q'_{15}	$0.97\times Q_{12}$	1^1		804
Q'_{16}	$0.91\times Q_{14}$	$17a^1$	998	981
Q'_{17}	$0.93\times Q_{18}$	$19a^1$		1100
Q'_{18}	$0.91\times Q_{17}$	$19b^1$		1085
Q'_{19}	$0.92\times Q_{19}$	$8b^1$	1140	1158
Q'_{20}	$0.75\times Q_{20}$, $0.09\times Q_{22}$, $0.08\times Q_{23}$	13^1 (3^1, $18a^1$)		1305
Q'_{21}	$0.24\times Q_{22}$, $0.10\times Q_{23}$, $0.64\times Q_{26}$	$18b^1$ (3^1, $18a^1$)		1400
Q'_{22}	$0.95\times Q_{21}$	$18a^1$	1200	1245
Q'_{23}	$0.18\times Q_{20}$, $0.57\times Q_{22}$, $0.17\times Q_{23}$	3^1 (13^1, $18a^1$)		1295
Q'_{24}	$0.99\times Q_{24}$	$18b^1$		1444
Q'_{25}	$0.08\times Q_{22}$, $0.62\times Q_{23}$, $0.24\times Q_{25}$	$18a^1$ ($9b^1$, 3^1)		1458
Q'_{26}	$0.95\times Q_{25}$	$9b^1$		1605
Q'_{27}	$0.99\times Q_{28}$	$7a^1$		3110
Q'_{28}	$0.97\times Q_{27}$	$20b^1$		3109
Q'_{29}	$1.00\times Q_{29}$	$20a^1$		3119
Q'_{30}	$0.98\times Q_{30}$	2^1		3121

[a] Normal modes of *p*-ClFPh in the S_1 state.
[b] Normal modes of *p*-ClFPh in the D_0 state.
[c] The scaling factor for the frequencies was 0.97.

the bands appearing at 419 and 998 cm^{-1} are in good agreement with the previously reported values of 421 and 987 cm^{-1}, which are assigned to the modes 14^1 and $17a^1$. The peaks observed in SEVI spectrum of *p*-ClFPh and vibrational modes are listed in Table IV.

F. Discussion

In order to comprehend the multimode mixing mechanism of vibrations (the Duschinsky rotation) in S_0, S_1 and D_0 states during the excitation and ionization processes, the Duschinsky mixing analysis is performed. FIG. 9(a, b) show the Duschinsky matrices of *p*-ClFPh representing the vibrational mode relationship between S_0 and S_1 states, and between S_1 and D_0 states, respectively. The corresponding information of FIG. 9(a, b) is also summarized in Table II and Table III. The redder their color is which means that the vibrational mode description is purer. In FIG. 9(a), we can find that most of the 30 normal vibrational modes in the S_1 state are similar to those in the S_0 state and only 6 of 30 normal vibrational modes appear slightly Duschinsky mixing. In those modes, 4 of S_1 modes are a two-mode mixing in S_0 state, and 2 out of S_1 modes are a three-mode mixing in S_0 state with quite Duschinsky mixing. From Table II, it is not difficult to see that Q_{22}, Q_{23}, Q_{26} significantly contribute to the mode mixing, with mainly CH vibration and benzene ring vibration.

Compared to FIG. 9(a), the multi-mode mixing in

DOI:10.1063/1674-0068/cjcp2001005

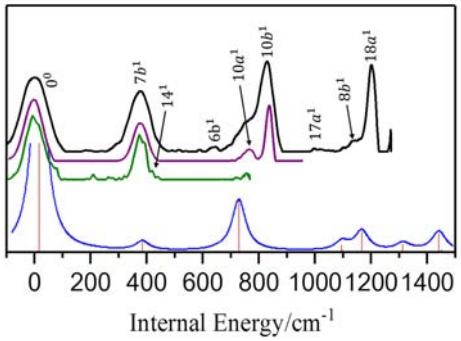

FIG. 8 Franck-Condon simulation of *p*-ClFPh in D_0 state at the level of aug-cc-pVTZ (blue line) in comparison with experimental spectra (black: 263.81nm, purple: 266.06 nm, green: 267.32 nm).

TABLE IV The vibration assignments of *p*-ClFPh observed in the D_0 state (in cm^{-1}).

Assignments	Shift from the ground state of D_0
0^0	0
$7b^1$	382
141	419
$6b^1$	645
$10a^1$	765
$10b^1$	832
$17a^1$	998
$8b^1$	1140
$18a^1$	1200

FIG. 9(b) is slightly serious. There are 20 out of D_0 modes exhibiting a ground state character ($\geq$95%) (see Table III). Also 6 of 30 normal vibrational modes appear to be slightly Duschinsky mixing. Specifically, 3 of D_0 modes are a two-mode mixing in S_1 state, and 3 out of D_0 modes are a three-mode mixing in S_1 state with quite Duschinsky mixing. Among them, Q_{22} and Q_{23} make significant contribution to the mode mixing, being associated with CH vibration and benzene ring vibration.

The photoelectron angular distribution (PAD) is obtained by integrating the intensity of the Abel-inverted image. The PADs in two-photon ionization with linearly polarized light are generally described by the function [34, 35]:

$$I(\theta) = k[1 + \beta_2 P_2(\theta) + \beta_4 P_4(\theta)] \quad (2)$$

where θ is the angle between the electron velocity vector and the laser polarization direction in the laboratory frame, k is a normalization constant proportional to the total photoionization cross-section, β_2 and β_4 are the anisotropy parameters associated with the second- and fourth-order Legendre polynomials P_2 and P_4, respectively, which can be determined by fitting Eq.(2).

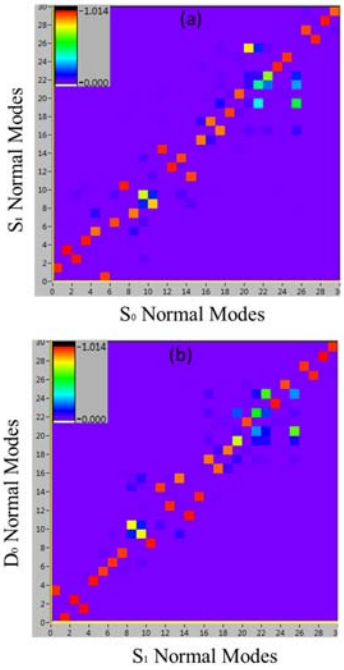

FIG. 9 The matrix representations of the Duschinsky analysis correlating (a) the ground state S_0 normal modes and the excited state S_1 normal modes of *p*-ClFPh, and (b) the excited state S_1 normal modes and the ground state D_0 normal modes of *p*-ClFPh.

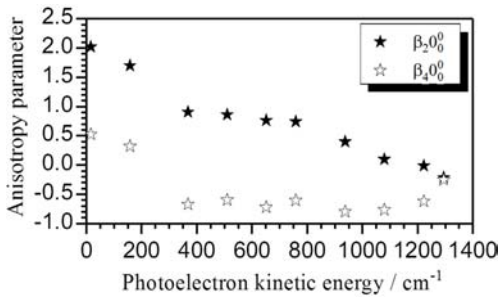

FIG. 10 The photoelectron angular anisotropy parameters (β_2 and β_4) obtained from the images pumping by S_1 0_0^0 level as shown in FIG. 6 as a function of PKE. The solid and hollow symbols indicate β_2 and β_4 values, respectively.

The PAD is determined by photoelectron scattering wave, which varies with the vibration dynamics of photoelectron kinetic energy (PKE) and ionized cations. The energy dependence of anisotropy parameters on PKE is shown in FIG. 10. The β_2 decreases with the increase of PKE, and the measured $\beta_2(E)$ for $D_0 \leftarrow S_1$ ionization process is negative when the PKE>1200 cm^{-1} above the ionization threshold.

Near the ionization threshold, the value β_2 of *para*-difluorobenzene decreases rapidly with the increase of PKE until it becomes negative, and it is suggested that the behavior of PAD trend near the ionization threshold is a consequence of the shape resonance. They concluded that the shape resonance was caused

DOI:10.1063/1674-0068/cjcp2001005

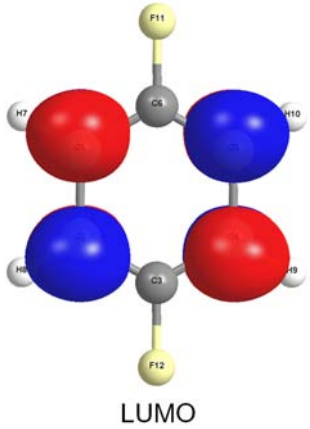

FIG. 11 The LUMO π^* orbital of *para*-difluorobenzene.

by the MO π^* orbital with high order angular momentum quantum number (l>1) [36–38]. This resonance was related to a π_g^* (LUMO)←π_u (HOMO) transition, which clearly showed the essential characteristics of dπ_g [39]. FIG. 11 shows the LUMO π^* orbital of *para*-difluorobenzene. To compare with the case of *p*-ClFPh (see FIG. 2), π^* antibonding (S_1 state) is similar to *para*-difluorobenzene. The LUMO π^* orbital of *p*-ClFPh in the ionization of D_0←S_1 exhibits a clear l=3 character. Considering the shape resonance from the perspective of trapping by a centrifugal barrier due to the relatively high (l=3) in this case, a significantly larger centrifugal barrier exists in the state and the value of the continuous resonant wavefunction effectively captures the electron at a short range. Therefore, it indicates that this behavior of PAD trend near threshold in *p*-ClFPh should be a consequence of the shape resonance. All values of β_2 and β_4 for the following excitation of various vibrational intermediate states are available in Table S5 (supplementary materials).

IV. CONCLUSION

We perform high-level theoretical prediction of the spectra and energy properties of *p*-ClFPh. The infrared spectrum in S_0 state of *p*-ClFPh is also studied, the vibrational modes of which are identified. According to the UV absorption spectrum, we get the transition probability mainly from HOMO to LUMO transition. Based on REMPI and SEVI spectroscopy and theoretical calculations, the geometric structures and vibrational frequencies of *p*-ClFPh in the first excited state of neutral and ground state of cationic are studied in detail. The REMPI spectrum of *p*-ClFPh gives the S_1←S_0 electronic transition energy, (36302±4) cm^{-1}. The S_1 band assignment based on RCIS with a basis set of aug-cc-pVTZ is quite appropriate in the aid of Franck-Condon simulation. In the 2C-R2PI SEVI spectra, the accurate AIP is obtained to be (72937±8) cm^{-1} of *p*-ClFPh through extrapolation to the ionization threshold. The vibrational frequencies in D_0 state calculated at the B3LYP/aug-cc-pVTZ level are in excellent agreement with the experimental ones and give the unambiguous assignment. More quite Duschinsky mixing existing in the D_0←S_1 ionization compared to that in the S_1←S_0 excitation indicates that more rotation of the vibrational coordinates occurs for the D_0←S_1 ionization than for the S_1←S_0 excitation.

Supplementary materials: DFT calculated coordinates, vibrational frequencies and corresponding desriptions of *p*-ClFPh in S_0, S_1 and D_0 states are shown.

V. ACKNOWLEDGMENTS

This work was supported by the National Natural Science Foundation of China (No.11674003, No.21873003, No.21503003, No.11704004, and No.61475001), Anhui Natural Science Foundation (No.1908085QA17). We also acknowledge additional support from Special Program for Applied Research on Super Computation of the NSFC-Guangdong Joint Fund (the second phase) (No.U1501501) and Super Computation Center of Shenzhen.

[1] S. Sinkkonen and J. Paasivirta, Chemosphere **40**, 943 (2000).
[2] M. S. Burger, J. L. Torino, and S. Swaminathan, Environ. Mol. Mutagen. **38**, 1 (2001).
[3] F. Zhang, H. R. Cheng, Z. W. Wang, X. P. Lv, Z. M. Zhu, G. Zhang, and X. M. Wang, Atmos. Environ. **86**, 193 (2014).
[4] M. Pera-Titus, V. García-Molina, M. A. Baños, J. Giménez, and S. Esplugas, Appl. Catal. B **47**, 219 (2004).
[5] R. Nilsson, G. Swanbeck, and G. Wennersten, Pholochem. Photobiol. **22**, 183 (1975).
[6] M. Czaplicka, Sci. Total. Environ. **322**, 21 (2004).
[7] K. H. Wang, Y. H. Hsieh, M. Y. Chou, and C. Y. Chang, Appl. Catal. B **21**, 1 (1999).
[8] K. L. Han and G. Z. He, J. Photochem. Photobiol. C **8**, 55 (2007).
[9] J. Murakami, K. Kaya, and M. Ito, J. Chem. Phys. **72**, 3263 (1980).
[10] A. Gaber, M. Riese, F. Witte, and J. Grotemeyer, Phys. Chem. Chem. Phys. **11**, 1628 (2009).
[11] O. A. Borg, Y. Y. Liu, P. Persson, S. Lunell, D. Karlsson, M. Kadi, and J. Davidsson, J. Phys. Chem. A **110**, 7045 (2006).
[12] Y. J. Liu, P. Persson, and S. Lunell, J. Phys. Chem. A **108**, 2339 (2004).
[13] X. P. Zhang, Z. R. Wei, W. B Lee, T. J. Chao, and K. C. Lin, Chemphyschem. **9**, 1721 (2008).
[14] W. Z. Li, S. F. Chen, and Y. J. Liu, J. Chem. Phys. **134**, 114303 (2011).

DOI:10.1063/1674-0068/cjcp2001005

[15] Y. J. Liu, P. Persson, H. O. Karlsson, S. Lunell, M. Kadi, D. Karlsson, and J. Davidsson, J. Chem. Phys. **120**, 6502 (2004).
[16] B. Liu, H. Zhao, X. Lin, X. Li, M. Gao, L. Wang, and W. Wang, Chem. Phys. Lett. **692**, 353 (2018).
[17] C. J. Hammond and K. L. Reid, Phys. Chem. Chem. Phys. **10**, 6762 (2008).
[18] C. Y. Ng, Annu. Rev. Phys. Chem. **65**, 197 (2014).
[19] K. L. Reid, Int. Rev. Phys. Chem. **27**, 607 (2008).
[20] Y. Numata, Y. Ishii, M. Watahiki, I. Suzuka, and M. Ito, J. Phys. Chem. **97**, 4930 (1993).
[21] W. D. Tuttle, A. M. Gardner, and T. G. Wright, Chem. Phys. Lett. **684**, 339 (2017).
[22] S. G. Lisa and P. Ausloos, J. Am. Chem. Soc. **100**, 6027 (1978).
[23] D. J. Kemp, L. E. Whalley, W. D. Tuttle, A. M. Gardner, B. T. Speake, and T. G. Wright, Phys. Chem. Chem. Phys. **20**, 12503 (2018).
[24] Z. Qin, N. Ma, Y. Ren, X. Zheng, G. Yao, X. Zhang, and Z. Cui, J. Quant. Spectrosc. Radiat. Transfer. **224**, 107 (2019).
[25] Z. Qu, C. Li, Z. Qin, X. Zheng, G. Yao, X. Zhang, and Z. Cui, Rev. Sci. Instrum. **86**, 063106 (2015).
[26] V. Dribinski, A. Ossadtchi, V. A. Mandelshtam, and H. Reisler, Rev. Sci. Instrum. **73**, 2634 (2002).
[27] G. Scalmani, V. Barone, B. Mennucci, G. A. Petersson, H. Nakatsuji, M. Caricato, X. Li, H. P. Hratchian, A. F. Izmaylov, J. Bloino, G. Zheng, J. L. Sonnenberg, M. Hada, M. Ehara, K. Toyota, R. Fukuda, J. Hasegawa, M. Ishida, T. Nakajima, Y. Honda, O. Kitao, H. Nakai, T. Vreven, J. A. Montgomery, J. E. Peralta, F. Ogliaro, M. Bearpark, J. J. Heyd, E. Brothers, K. N. Kudin, V. N. Staroverov, R. Kobayashi, J. Normand, K. Raghavachari, A. Rendell, J. C. Burant, S. S. Iyengar, J. Tomasi, M. Cossi, N. Rega, J. M. Millam, M. Klene, J. E. Knox, J. B. Cross, V. Bakken, C. Adamo, J. Jaramillo, R. Gomperts, R. E. Stratmann, O. Yazyev, A. J. Austin, R. Cammi, C. Pomelli, J. W. Ochterski, R. L. Martin, K. Morokuma, V. G. Zakrzewski, G. A. Voth, P. Salvador, J. J. Dannenberg, S. Dapprich, A. D. Daniels, O. Farkas, J. B. Foresman, J. V. Ortiz, J. Cioslowski, and D. J. Fox, *Gaussian 09, revision D.01*, Wallingford CT: Gaussian, Inc. (2009).
[28] T. Yanai, D. P Tew, and N. C. Handy, Chem. Phys. Lett. **393**, 51 (2004).
[29] I. Pugliesi and K. Muller-Dethlefs, J. Phys. Chem. A **110**, 4657 (2006).
[30] E. B. Wilson, Phys. Rev. **45**, 706 (1934).
[31] T. Lu and F. Chen, J. Comput. Chem. **33**, 580 (2012).
[32] T. Cvitaš and J. M. Hollas, Mol. Phys. **18**, 261 (1970).
[33] W. D. Tuttle, A. M. Gardner, L. E. Whalley, and T. G. Wright, J. Chem. Phys. **146**, 244310 (2017).
[34] Y. Ogi, H. Kohguchi, D. Niu, K. Ohshimo, and T. Suzuki, J. Phys. Chem. A **113**, 14536 (2009).
[35] C. N. Yang, Phys. Rev. **74**, 764 (1948).
[36] S. M. Bellm, J. A. Davies, P. T. Whiteside, J. Guo, I. Powis, and K. L. Reid, J. Chem. Phys. **122**, 224306 (2005).
[37] S. M. Bellm and K. L. Reid, Phys. Rev. Lett. **91**, 263002 (2003).
[38] M. Staniforth, S. Daly, K. L. Reid, and I. Powis, J. Chem. Phys. **139**, 064304 (2013).
[39] H. Xu, U. Jacovella, B. Ruscic, S. T. Pratt, and R. R. Lucchese, J. Chem. Phys. **136**, 154303 (2012).

DOI:10.1063/1674-0068/cjcp2001005

Supplementary materials for "Experimental and theoretical study on p-chlorofluorobenzene in the S_0, S_1 and D_0 states"

Jianan Fan, Tingting Cui, Zhengbo Qin[a)], Xianfeng Zheng[a)], and Zhifeng Cui

Anhui Province Key Laboratory of Optoelectric Materials Science and Technology, Department of Physics, Anhui Normal University, Wuhu, Anhui 241000, China

[a)] Corresponding authors: Email: wave0403@163.com (Z.B.Q.), xfzheng@mail.ahnu.edu.cn(X.F.Z.)

Table S1

Cartesian coordinates of p-ClFPh in neutral ground and ionic ground states calculated from B3LYP/aug-cc-pVTZ calculations. Cartesian coordinates of p-ClFPh in neutral first excited state calculated from RCIS-B3LYP/aug-cc-pVTZ calculations.

[C_6H_4ClF]	**C_{2v}**	**S_0**	**B3LYP/aug-cc-pVTZ**		
Center	Atomic	Atomic	Coordinates (Angstroms)		
Number	Number	Type	X	Y	Z
1	*6*	*0*	0.000000	1.210801	-1.131802
2	*6*	*0*	0.000000	1.209129	0.258006
3	*6*	*0*	0.000000	0.000000	0.940599
4	*6*	*0*	0.000000	-1.209129	0.258006
5	*6*	*0*	0.000000	1.210801	-1.131802
6	*6*	*0*	0.000000	0.000000	-1.800779
7	*1*	*0*	0.000000	2.135300	-1.690829
8	*1*	*0*	0.000000	2.140080	0.805255
9	*1*	*0*	0.000000	-2.140080	0.805255
10	*1*	*0*	0.000000	-2.135300	-1.690829
11	*9*	*0*	0.000000	0.000000	-3.151044
12	*17*	*0*	0.000000	0.000000	2.692775

[C_6H_4ClF]	**C_{2v}**	**D_0**	**B3LYP/aug-cc-pVTZ**		
Center	Atomic	Atomic	Coordinates (Angstroms)		
Number	Number	Type	X	Y	Z
1	*6*	*0*	0.000000	1.245158	-1.109867
2	*6*	*0*	0.000000	1.244391	0.254302
3	*6*	*0*	0.000000	0.000000	0.947886
4	*6*	*0*	0.000000	-1.244391	0.254302
5	*6*	*0*	0.000000	-1.245158	-1.109867
6	*6*	*0*	0.000000	0.000000	-1.780221
7	*1*	*0*	0.000000	2.157796	-1.689070
8	*1*	*0*	0.000000	2.165885	0.818149
9	*1*	*0*	0.000000	-2.165885	0.818149
10	*1*	*0*	0.000000	-2.157796	-1.689070
11	*9*	*0*	0.000000	0.000000	-3.082850
12	*17*	*0*	0.000000	0.000000	2.632252

[C_6H_4ClF]	**C_{2v}**	**S_1**	**RCIS/aug-cc-pVTZ**		
Center	Atomic	Atomic	Coordinates (Angstroms)		
Number	Number	Type	X	Y	Z
1	*6*	*0*	0.000000	1.240381	-1.133095
2	*6*	*0*	0.000000	1.239700	0.271281
3	*6*	*0*	0.000000	0.000000	0.940984
4	*6*	*0*	0.000000	-1.239700	0.271281
5	*6*	*0*	0.000000	-1.240381	-1.133095
6	*6*	*0*	0.000000	0.000000	-1.787109
7	*1*	*0*	0.000000	2.142627	-1.707054
8	*1*	*0*	0.000000	2.148569	0.833202
9	*1*	*0*	0.000000	-2.148569	0.833202
10	*1*	*0*	0.000000	-2.142627	-1.707054
11	*9*	*0*	0.000000	0.000000	-3.090768
12	*17*	*0*	0.000000	0.000000	2.646067

Table S2

Vibrational frequencies of p-ClFPh in S_0, S_1 and D_0 states (in cm^{-1}). The S_0 and D_0 states are calculated by the B3LYP/aug-cc-pVTZ method. And the S_1 state is calculated by the RCIS-B3LYP/aug-cc-pVTZ method. A scaling factor of 0.97 was employed to the frequencies.

		S_0			*S_1*		*D_0*		
No	Mode	Sym.	Theo.	Exp.	Theo.	Exp.	Theo.	Exp.	Mode description [a]
Q_1	11^1	B1	123		110		100		oop; CCl bend
Q_2	$9a^1$	B2	254		281		268		ip; CCl bend
Q_3	$10a^1$	B1	326		275	261	270		oop; ring deform
Q_4	$7b^1$	A1	364		365	344	370	382	ip; CCl stretch
Q_5	14^1	B2	412		428	396	412	419	ip; CF scissor
Q_6	$16a^1$	A2	416		71		358		oop; ring deform
Q_7	$16b^1$	B1	498		511	488	497		oop; ring deform
Q_8	$6b^1$	A1	617		660		639	645	ip; ring stretch
Q_9	$6a^1$	B2	624	632	585	546	573		ip; ring stretch
Q_{10}	$16a^1$	B1	693		601	623	702		oop; ring deform
Q_{11}	$10a^1$	A2	800		599		774	765	ip; CH torsion
Q_{12}	1^1	A1	810		850	863	804		ip; breathing
Q_{13}	$10b^1$	B1	829	823	750	765	855	832	oop; CH wag
Q_{14}	$17a^1$	B1	935		813	795	981	998	oop; CH torsion
Q_{15}	5^1	A2	948		676	703	977		oop; CH torsion
Q_{16}	12^1	A1	1002	1012	1036	1033	965		ip; ring stretch
Q_{17}	$19b^1$	A1	1064		1136	1142	1085		ip; ring stretch
Q_{18}	$19a^1$	B2	1082	1088	1104	1109	1100		ip; ring stretch
Q_{19}	$8b^1$	A1	1141	1152	1203	1197	1158	1140	ip; ring stretch
Q_{20}	13^1	A1	1212	1229	1340	1340	1305		ip; CF stretch
Q_{21}	$18a^1$	B2	1274	1267	1760		1245	1200	ip; CH bend
Q_{22}	3^1	B2	1278	1286	1416		1295		ip; CH rock
Q_{23}	$18a^1$	B2	1389	1402	1446		1458		ip; ring deform
Q_{24}	$18b^1$	A1	1477	1487	1535		1444		ip; CH rock
Q_{25}	$9b^1$	A1	1581		1662		1605		ip; CH bend
Q_{26}	$18b^1$	B2	1583	1593	1214	1232	1400		ip; CH bend
Q_{27}	$20b^1$	A1	3099	3076	3278		3109		ip; CH stretch
Q_{28}	$7a^1$	B2	3101	3103	3273		3110		ip; CH stretch
Q_{29}	$20a^1$	B2	3112		3291		3119		ip; CH stretch
Q_{30}	2^1	A1	3113		3295		3121		ip; CH stretch

[a] oop, out-of-plane; ip, in- plane.

Table S3

The comparison of experimental values with calculated values, and corresponding vibration description of p-ClFPh in S_0 state. The calculated values with a scaling factor of 0.97.

Calc. freq.	Obs.freq	Mode description [a]
624	632	ip; ring stretch
829	823	oop; CH wag
1002	1012	ip; ring stretch
1082	1088	ip; ring stretch
1141	1152	ip; ring stretch
1212	1229	ip; CF stretch
1274	1267	ip; CH bend
1278	1286	ip; CH rock
1389	1402	ip; CH scissor
1477	1487	ip; CH rock
1583	1593	ip; CH bend
3099	3076	ip; CH stretch
3101	3103	ip; CH stretch

[a] oop, out-of-plane; ip, in-plane;

Table S4

Theoretical harmonic frequencies (cm^{-1}) and normal vibrational modes in the p-ClFPh ground state (S_0), first excited state (S_1) of neutral and ground state of cation (D_0). All frequencies are calculated using aug-cc-pVTZ basis set without using scaling factor.

Mode	S_0 (B3LYP)		S_1 (RCIS-B3LYP)		D_0 (B3LYP)	
	Freq.		Freq.		Freq.	
11^1	127	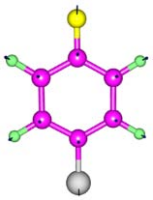	114	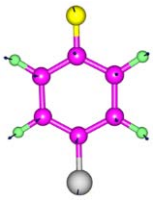	103	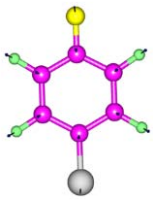
$9a^1$	262	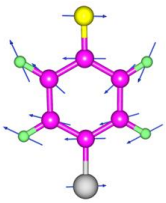	289	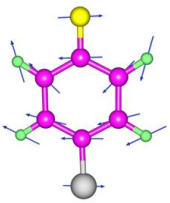	276	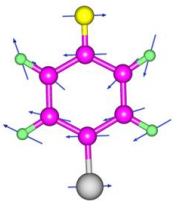
$10a^1$	326		284	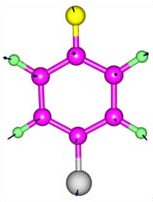	278	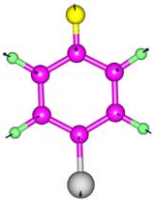
$7b^1$	376	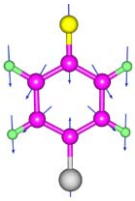	377		382	
14^1	424	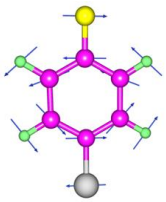	442	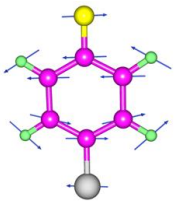	425	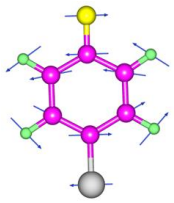
$16a^1$	429	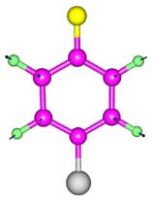	73	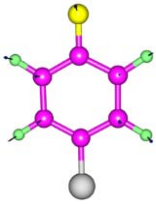	370	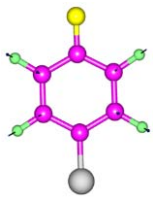
$16b^1$	513	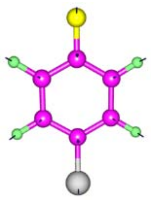	526	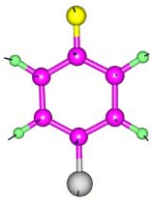	512	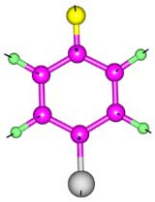

$6b^1$	636	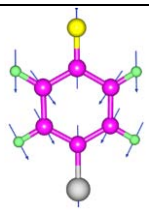	681	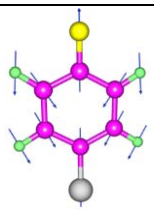	658	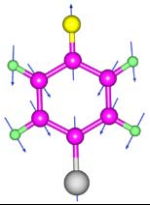
$6a^1$	643	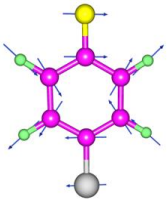	603	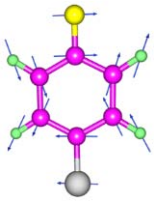	590	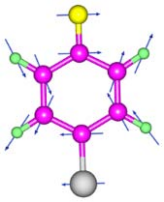
$16a^1$	714	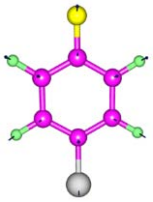	618	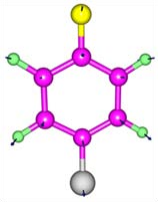	724	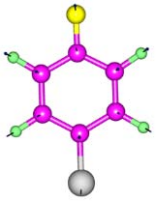
$10a^1$	825	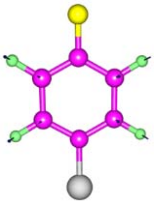	619	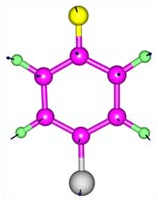	798	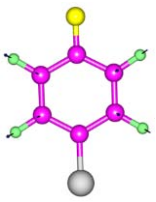
1^1	835	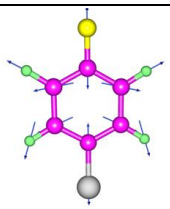	876	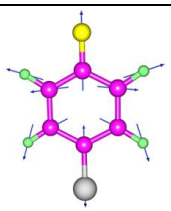	829	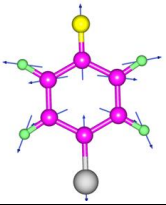
$10b^1$	855	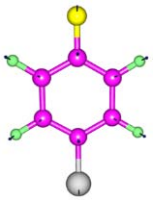	774	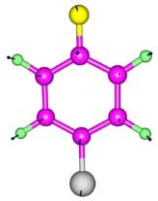	882	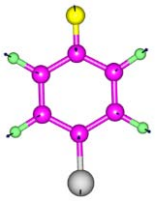
$17a^1$	964		838	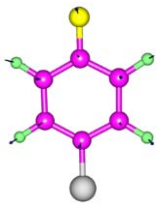	1012	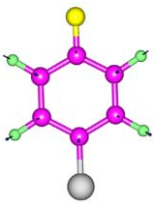
5^1	977	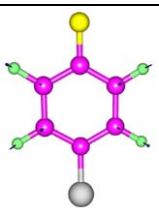	697	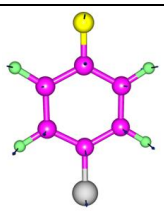	1007	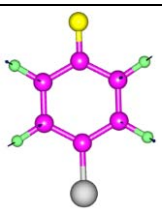

12^1	1033	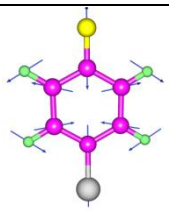	1068	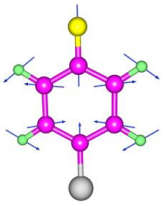	995	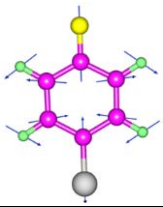
$19b^1$	1097	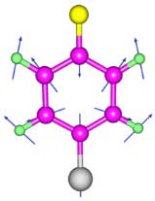	1171		1119	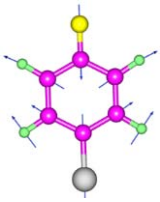
$19a^1$	1115		1138	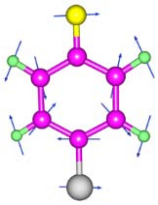	1134	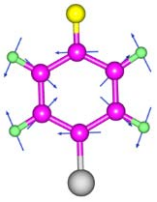
$8b^1$	1177	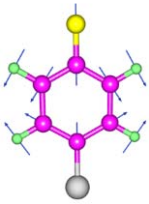	1241	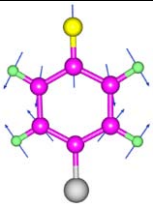	1194	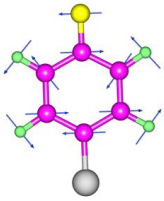
13^1	1249	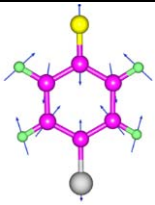	1382	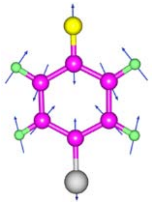	1345	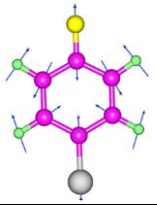
$18a^1$	1313		1815	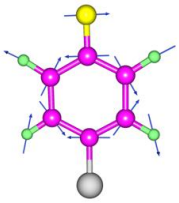	1284	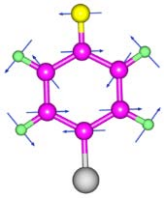
3^1	1317	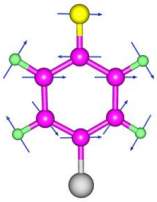	1460	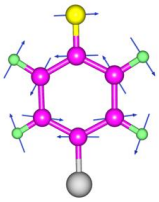	1335	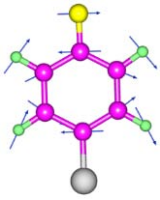
$18a^1$	1432	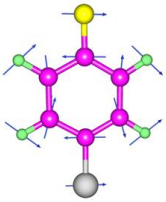	1491	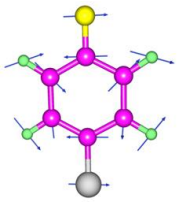	1503	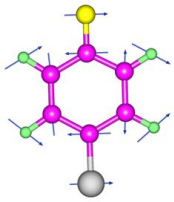

$18b^1$	1523	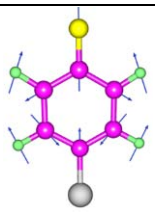	1584	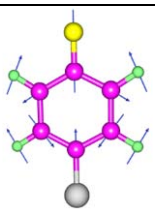	1489	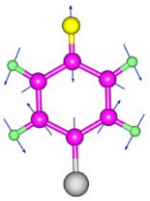
$9b^1$	1630	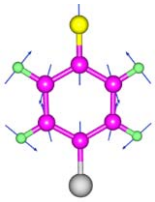	1713	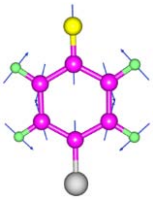	1654	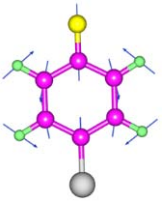
$18b^1$	1632	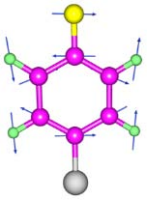	1251	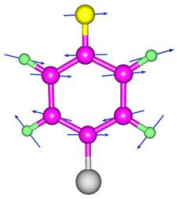	1444	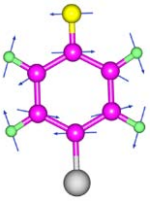
$20b^1$	3195	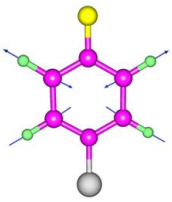	3379	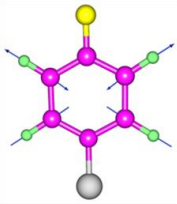	3205	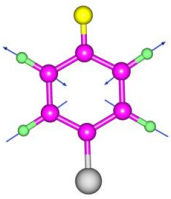
$7a^1$	3197	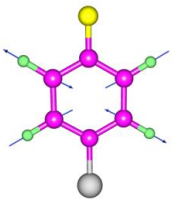	3374	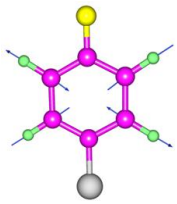	3206	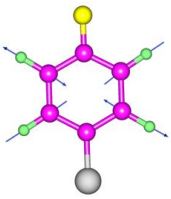
$20a^1$	3208	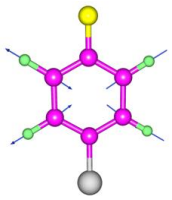	3393	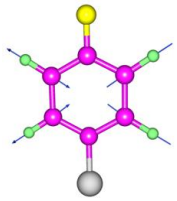	3216	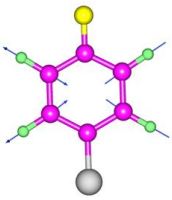
2^1	3210	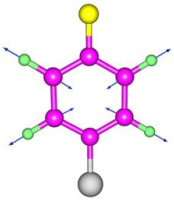	3397	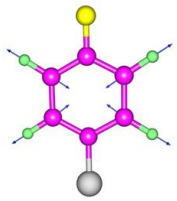	3217	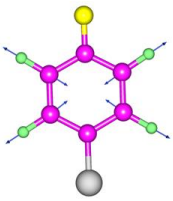

Table S5

Anisotropy parameters (β_2, β_4) used for fitting the photoelectron angular distributions from the ionization of excited-state p-ClFPh via 0_0^0 energy level in the S_1 state

excitation (cm^{-1})	ionization (cm^{-1})	0^0	
		β_2	β_4
36302	37347	0.8612	-0.5949
0_0^0	37571	0.4177	-1.0352
	37610	0.2412	0.7473
	37692	0.2459	0.9556
	37762	0.1399	0.6869
	37839	-0.1537	0.7858
	37906	-0.2182	1.0300
	37978	-0.2492	0.8901
	38030	-0.2295	-0.2639
	38121	-0.3489	0.3708